

Measurement report: Airborne measurements of NO_x fluxes over Los Angeles during the RECAP-CA 2021 campaign

Clara M. Nussbaumer^{1,2}, Bryan K. Place², Qindan Zhu³, Eva Y. Pfannerstill⁴, Paul Wooldridge², Benjamin C. Schulze⁵, Caleb Arata⁴, Ryan Ward⁵, Anthony Bucholtz⁶, John H. Seinfeld⁵, Allen H. Goldstein^{4,7}, and Ronald C. Cohen^{2,3}

¹Department of Atmospheric Chemistry, Max Planck Institute for Chemistry, 55128 Mainz, Germany

²Department of Chemistry, University of California, Berkeley, Berkeley, CA 94720, USA

³Department of Earth and Planetary Science, University of California, Berkeley, Berkeley, CA 94720, USA

⁴Department of Environmental Science, Policy, and Management, University of California, Berkeley, Berkeley, CA 94720, USA

⁵Department of Environmental Science and Engineering, California Institute of Technology, Pasadena, CA 91125, USA

⁶Department of Meteorology, Naval Postgraduate School, Monterey, CA 93943, USA

⁷Department of Civil and Environmental Engineering, University of California, Berkeley, Berkeley, CA 94720, USA

Correspondence: Clara M. Nussbaumer (clara.nussbaumer@mpic.de) and Ron C. Cohen (rccohen@berkeley.edu)

Abstract.

Nitrogen oxides ($\text{NO}_x \equiv \text{NO} + \text{NO}_2$) are involved in most atmospheric photochemistry, including the formation of tropospheric ozone (O_3). While various methods exist to accurately measure NO_x concentrations, it is still a challenge to quantify the source and flux of NO_x emissions. We present airborne measurements of NO_x and winds used to infer the emission of NO_x across Los Angeles. The measurements were obtained during the research aircraft campaign RECAP-CA (Re-Evaluating the Chemistry of Air Pollutants in CALifornia) in June 2021. Geographic allocations of the fluxes are compared to the NO_x emission inventory from the California Air Resources Board (CARB). We find that the NO_x fluxes have a pronounced weekend effect and are highest in the Eastern part of the San Bernardino valley. The comparison of the RECAP-CA and the modeled CARB NO_x fluxes suggest the modeled emissions are higher than expected near the coast and in downtown Los Angeles and lower than expected further inland in the Eastern part of the San Bernardino valley.

1 Introduction

Nitrogen oxides (NO_x), representing the sum of nitric oxide (NO) and nitrogen dioxide (NO_2), are hazardous pollutants and precursor to tropospheric ozone, which is known to have adverse health effects on humans and plants (Boningari and Smirniotis, 2016; Mills et al., 2018; Nuvolone et al., 2018; CARB, 2022b). NO_x is emitted from some natural sources including soil, microbial activity and lightning, but mostly from anthropogenic combustion sources, such as electricity generation facilities and motor vehicles, with the latter dominating in urban environments (Delmas et al., 1997; Pusede et al., 2015). Densely populated cities, such as the megacity Los Angeles, often suffer from poor air quality leading to increases in respiratory diseases and premature mortality (Stewart et al., 2017). Air quality monitoring, public policy and new emission control technologies have

been developed and implemented to assess, guide and manage emissions, leading to healthier air in cities (CARB, 2022b).
20 Significant reductions in NO_x and other primary pollutants have occurred in the U.S. and specifically in Los Angeles over
the past decades (e.g. Qian et al. (2019); Nussbaumer and Cohen (2020); EPA (2022a)). However, ozone exceedances of the
national ambient air quality standard (NAAQS) of 0.070 ppm (8-hr maximum) are still frequent in Los Angeles which the
American Lung Association (2022) found to have the highest ozone pollution in all of the United States (South Coast Air
Quality Management District, 2017; EPA, 2022c). In the summer months June - September of 2021, O_3 exceeded the NAAQS
25 on more than half the days. Exceedances were even more frequent in 2020, demonstrating that further precursor reductions are
imperative (EPA, 2022b).

The combination of emission inventories with models provides insight into the emission reductions needed to achieve healthy
air. It helps us understand atmospheric dynamics which includes the transport of emitted trace gases from their source through
the atmosphere, their deposition to the earth's surface and the oxidation processes they are involved in. Comparison of pre-
30 dicted concentrations of chemicals with this type of combined modeling system provides a guide for the needed reductions in
emissions to protect public health. Errors and biases in any part of this system can lead to incorrect estimates of the amount of
reduction needed to achieve a particular goal. Fujita et al. (2013) pointed towards the problem of biased emission inventories
regarding future predictions of ozone, naming underestimations in early VOC (volatile organic compound) SoCAB (South
Coast Air Basin) emission inventories and hence modeled VOC/ NO_x that did not match the atmosphere as a key bias in
35 understanding ozone chemistry.

Direct observational mapping of emissions would allow a more straightforward evaluation of the accuracy of emission in-
ventories without requiring untangling potential errors in emissions from those of transport or chemistry. Until recently, such
measurements have been rare because of the difficulty of obtaining and interpreting measurements of emissions in heteroge-
neous urban environments and especially the difficulty of mapping emissions over the spatial scales needed to assess the full
40 complement of urban processes. Recently, several experiments have overcome these challenges, measuring NO_x and VOC
fluxes using aircraft platforms.

Airborne studies on VOC fluxes include Karl et al. (2013) and Misztal et al. (2014) who present fluxes of biogenic VOCs
based on research flights during the CABERNET (California Airborne BVOC Emission Research in Natural Ecosystem Tran-
sects) campaign over Californian oak forests in June 2011. Yuan et al. (2015) determined CH_4 and VOC emissions from two
45 shale gas production plants in the Southern United States based on aircraft measurements in summer 2013. Yu et al. (2017)
derived isoprene and monoterpene fluxes during the airborne Southeast Atmosphere Study above the U.S. in 2013. Other stud-
ies presenting VOC fluxes based on aircraft measurements include Karl et al. (2009), Conley et al. (2009), Kaser et al. (2015),
Wolfe et al. (2015), Gu et al. (2017) and Yu et al. (2017).

Nitrogen oxides fluxes based on airborne measurements are even less common than VOCs. Wolfe et al. (2015) reported NO_x
50 fluxes based on a measurement flight during the NASA SEAC⁴RS campaign in 2013. Vaughan et al. (2016) and Vaughan et al.
(2021) reported NO_x fluxes based on this method over the Greater London region during the OPFUE (Ozone Precursors Fluxes
in an Urban Environment) campaign in July 2014. They compared emission predictions from the National Atmospheric Emis-
sions Inventory with the calculated NO_x fluxes via wavelet transformation, which they found to be higher than the inventory

by up to a factor of 2, underlining the importance of emission inventory validation. Zhu et al. (2023) recently reported NO_x fluxes over the San Joaquin Valley of California based on the RECAP-CA (Re-Evaluating the Chemistry of Air Pollutants in CALifornia) aircraft campaign where NO_x from soils was identified as a key contributor to the overall emission.

In this paper, we present NO_x flux calculations via wavelet transformation from aircraft measurements of NO_x concentrations and the vertical wind speed during the RECAP-CA aircraft campaign over Los Angeles in June 2021. We provide footprint calculations for investigating the origin of the sampled air masses and compare our results to the emission inventory of the California Air Resources Board (CARB).

2 Observations and methods

2.1 RECAP-CA aircraft campaign

The RECAP-CA (Re-Evaluating the Chemistry of Air Pollutants in CALifornia) aircraft campaign took place in June 2021 over Los Angeles and the Central Valley of California with the campaign base in Burbank, California (34.20° N , 118.36° W) using the CIRPAS (Center for Interdisciplinary Remotely Piloted Aircraft Studies) Twin Otter aircraft. Details on the research aircraft (Figure S1) can be found in Reid et al. (2001) and Hegg et al. (2005). The ambient air was sampled with an inlet approximately 1 m above the aircraft nose at a sampling speed (aircraft speed) of around 60 m s^{-1} . The aircraft carried instruments for measurements of meteorological data, nitrogen oxides, volatile organic compounds and greenhouse gases. All flights were carried out between 11:00 and 18:00 local time (LT).

We focus on the measurements over Los Angeles which took place on three weekends (June 6, 12 and 19) and six weekdays (June 1, 4, 10, 11, 18 and 21) in 2021. The flight paths are shown in Figure 1a. All flights were carried out at an altitude of roughly 300 - 400 m above ground level, covering the coastal region of Los Angeles, parts of Santa Ana county, Los Angeles Downtown and the San Bernardino valley. Flight days were chosen to explore as wide a range of temperature as possible. In addition, about half the flights started with the Northwest-Southeast legs and the other half the coastal North-South legs to gain additional variation in temperature. For further analysis, we separated the covered area in four different segments, as shown in Figure 1b.

2.2 Meteorological measurements

The meteorological instruments on-board the CIRPAS Twin Otter research aircraft were previously described in Karl et al. (2013). Temperature was obtained by a Rosemount Sensor (Emerson Electric Co., St. Louis, Missouri, USA). Dew point temperature was measured by a DewMaster Chilled Mirror Hygrometer (Edgetech Instruments Inc., Hudson, Massachusetts, USA). Differential and barometric pressure sensors (Setra Systems Inc., Boxborough, Massachusetts, USA) were used to determine the pressure. GPS latitude, longitude, altitude, ground speed and track, as well as pitch, heading and roll angle were measured by a C-MIGITS (Miniature Integrated GPS (Global Positioning System)/INS (Inertial Navigation System) Tactical System) III (Systron Donner Inertial Division, Concord, California, USA). A radome flow angle probe provided the

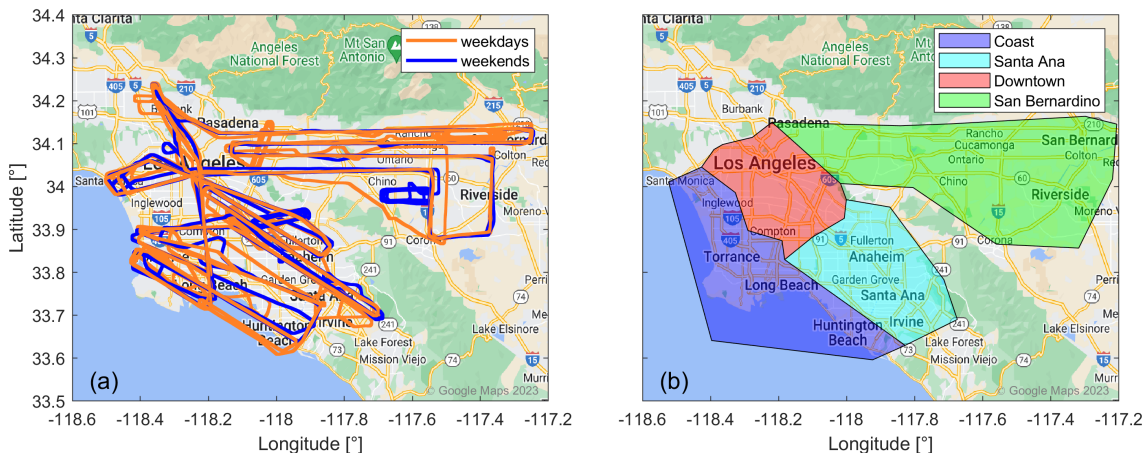


Figure 1. (a) Overview of the flight paths during the RECAP-CA campaign over Los Angeles in June 2021. Blue colors show weekend flights and orange colors show weekday flights. (b) Geographic separation of the covered area in four segments, including the coast (blue), parts of Santa Ana county (light blue), Downtown Los Angeles (red) and the San Bernardino valley (green). © Google Maps 2023.

85 true air speed and the 3D wind. The planetary boundary layer (PBL) height was determined from changes in water vapor and toluene concentrations, the dew point and temperature, which decrease rapidly at the boundary between the BL and the free troposphere (Pfanerstill et al., 2023). The aircraft crossed the top of the PBL at several times during each flight providing these direct observations.

2.3 NO_x measurements

90 NO_x measurements were carried out using a custom-built three-channel thermal dissociation laser-induced fluorescence (TD-LIF) instrument with a detection limit of ~ 15 pptv (10 s) (higher for higher resolution data) and a precision (2σ) of $< 7\%$ (Thornton et al., 2000). The instrument is described in detail in Thornton et al. (2000), Day et al. (2002) and Sparks et al. (2019). Briefly, NO₂ is excited in the first channel with a 532 nm Nd³⁺:YVO₄ laser (Explorer One XP, Spectra Physics). The fluorescence resulting from NO₂* de-excitation is detected by a photomultiplier tube as a signal which is approximately
 95 proportional to the ambient NO₂ mixing ratio. The proportionality arises because the fluorescence signal and the quenching of the fluorescence both scale with pressure. Calibration with an NO₂ gas standard (5.5 ppm; Praxair) was performed once an hour. The instrument background was determined every 20 minutes using scrubbed ambient air. NO is determined in the second channel through conversion to NO₂ by adding excess ozone (O₃). Reactive nitrogen species (NO_y \equiv NO_x, HNO₃, HONO, RONO₂, RO₂NO₂, ...) were detected through thermal dissociation at $\sim 500^\circ$ C to NO₂ in the third channel (Day et al.,
 100 2002). Ambient air was sampled at a flow rate of 6 l/min, equally divided into the three instrument channels.

2.4 NO_x flux calculations

The emission of a trace gas is characterized as a flux which is a mass emitted per area and time, e.g. mg m² h⁻¹. A flux F can be described as the covariance of the fluctuation in the vertical wind speed w' and the fluctuation in the concentration of the trace gas of interest c' , as shown in Eq. (1).

$$105 \quad F = \overline{w'c'} \quad (1)$$

Analyses of the covariance of winds and concentrations from tower-based or aircraft-based observations enable the determination of fluxes. With the eddy covariance method, the flux is directly calculated from the measurements as the mean of the product of the deviation of the vertical windspeed from the mean of the vertical wind speed and the deviation of the concentration analogously, as shown in Eq. (2) (e.g. Schaller et al. (2017); Desjardins et al. (2021)).

$$110 \quad \overline{w'c'} = \frac{1}{N} \sum_{x=1}^N (w_x - \bar{w})(c_x - \bar{c}) \quad (2)$$

Requirements for accurate fluxes with EC are stationary conditions and a vertically homogeneously mixed boundary layer. Typically an averaging time of at least 30 minutes is used to ensure the full spectrum of eddies are sampled (Schaller et al., 2017; Desjardins et al., 2021). The 30 minutes long averaging time is easily implementable for stationary tower installments. For aircraft observations, the high aircraft velocity and the associated rapid geographical change are inconsistent with the stationary requirement. An alternative is the flux calculation via wavelet transformation. This approach does not require the assumption of stationary conditions as it enables the determination of a flux localized both in time and frequency (Karl et al., 2013; Schaller et al., 2017). A discrete time series such as the vertical wind speed or the concentration of an atmospheric trace gas is convolved with a wavelet function $\psi_{a,b}(t)$ yielding the wavelet coefficient $W(a,b)$ according to Eq. (3) (Torrence and Compo, 1998; Thomas and Foken, 2005; Schaller et al., 2017; Desjardins et al., 2021).

$$120 \quad W(a,b) = \int_{-\infty}^{\infty} x(t)\psi_{a,b}(t)dt \quad (3)$$

The function $\psi_{a,b}(t)$, Eq. (4), a wavelet, scaled by a and shifted by b , controlling the frequency and the time of the wavelet, respectively. In our study, we use the complex Morlet wavelet ψ_M , Eq. (5), which is the product of a sine and a gaussian function, with $\omega_0 = 6$ and $u = \frac{t-b}{a}$ (Torrence and Compo, 1998; Metzger et al., 2013; Wolfe et al., 2018).

$$\psi_{a,b}(t) = \frac{1}{\sqrt{a}} \times \psi_M\left(\frac{t-b}{a}\right) \quad (4)$$

$$125 \quad \psi_M(u) = \pi^{-\frac{1}{4}} \times e^{-i\omega_0 u} \times e^{-\frac{u^2}{2}} \quad (5)$$

The expression $|W^2(a, b)|$ represents the power spectrum of the discrete time series, showing each scale a and translation b with the according amplitude. For two different time series, the product of the wavelet coefficients yields the cross power spectrum which when integrated across scales represents the covariance and, in case of the vertical wind speed and the trace gas concentration, the flux (Torrence and Compo, 1998; Metzger et al., 2013; Schaller et al., 2017). The flux is calculated
130 through wavelet transformation via Eq. (6).

$$\overline{w'c'} = \frac{\delta t}{C_\delta} \times \frac{\delta j}{N} \times \sum_{n=0}^{N-1} \sum_{j=0}^J \frac{[W_c(a, b) \times W_w^*(a, b)]}{a(j)} \quad (6)$$

C_δ is a reconstruction factor equal to 0.776 for the Morlet wavelet. N is the number of elements in the time series ($n = 0, 1, \dots, N$) with the time step δt and J is the number of scales ($j = 0, 1, \dots, J$) with the spacing δj (Metzger et al., 2013; Schaller et al., 2017; Desjardins et al., 2021). Both data pre-treatment (of the NO_x and meteorological data) and wavelet
135 analysis were performed following the procedure presented by Vaughan et al. (2021). The time stamp of the meteorological data was interpolated to the NO_x data time stamp with a resolution of 5 Hz. We generated flight segments as input for the wavelet analysis with a 10 km minimum length of continuous measurements. Observations above the boundary layer and thus in the free troposphere were excluded from our analysis as they are assumed to be out of contact with the surface below. Data with an aircraft roll angle larger than 8° or where the altitude changed by more than ~ 100 m across the 10 km were
140 excluded. Due to different inlet sampling locations and computer clocks, the NO_x measurements and the vertical wind speed measurements were slightly time shifted. This lag correction was quantified via the cross covariance of the two time series. The vertical wind speed was then shifted to the NO_x measurements according to the covariance peak. We used the median lag of all segments of the same flight day for the lag correction.

For the wavelet analysis, we followed the procedure described in detail in Torrence and Compo (1998). The wavelet trans-
145 form was calculated separately for the vertical wind speed fluctuation w' and the NO_x concentration fluctuation c' . We used the wavelet software provided by C. Torrence and G. Compo, with the Morlet wavelet ψ_M (described in Eq. (5)), the time step $\delta t = 0.2 \text{ s}^{-1}$, a scale spacing $\delta j = 0.25$ and a scale number of $J = \log_2\left(\frac{N\delta t}{j_{min}}\right) \times \frac{1}{\delta j}$ (default value, $j_{min} = 2 \times \delta t$). For example, there would be 36 scales for a segment with 1000 data points. The cross spectrum was obtained through the sum of the product of the real parts of the wavelet transform for c' and w' and the product of the imaginary parts, which gave the NO_x
150 flux via the weighted sum over all scales according to Eq. (24) in Torrence and Compo (1998). Due to edge effects, the error is particularly high at the beginning and end of each segment which is described by the cone of influence (COI) (Torrence and Compo, 1998). We have discarded data points for which more than 80 % of the spectral information is located within the COI. Note that approximately 50 % of the data points are lost due to edge effects, likely due to short segment lengths and frequent calibrations. For our analysis, we used the 2 km moving mean of the NO_x flux. Figure 2a shows the discrete time series of the
155 NO_x concentration and the vertical wind speed for one segment on 6 June with a length of 30.0 km. The x axis shows the time in seconds from the start of the segment (~ 9 min). Figure 2b shows the cross power spectrum of c' and w' , with red colors representing positive and blue colors representing negative amplitudes, and the cone of influence by the black dashed line. The 2 km moving mean of the resulting NO_x flux is presented in Figure 2c.

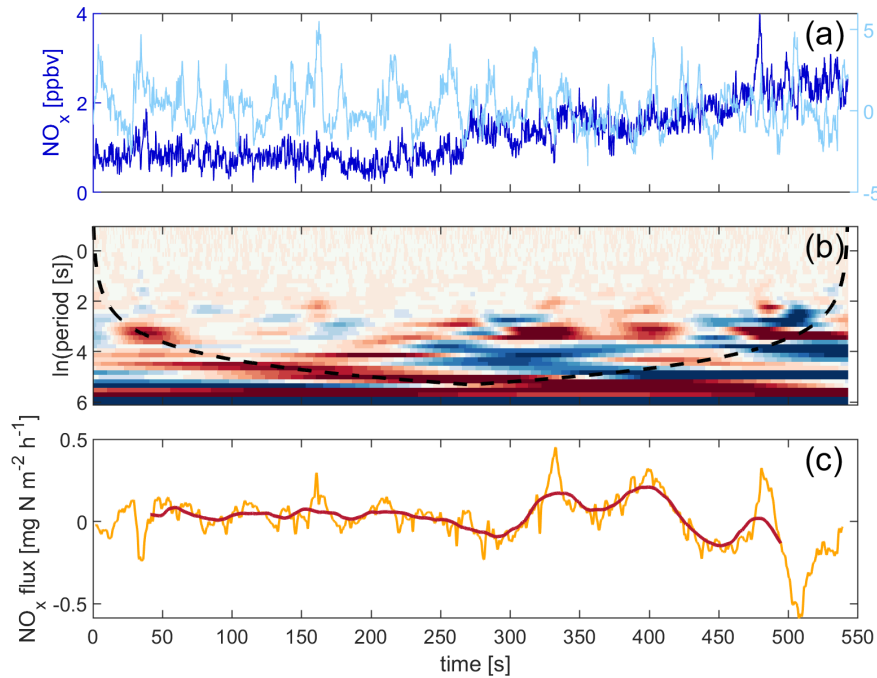


Figure 2. (a) Discrete time series of the NO_x concentration (dark blue) and the vertical wind speed (light blue) for a segment on 6 June. (b) Cross power spectrum with 41 scales and 2777 translations, the latter equaling the number of points in the segment. Red colors represent positive and blue colors represent negative amplitudes. (c) The resulting NO_x flux (orange) and the 2 km moving mean (red).

In Figure S2 of the Supplement we present an example covariance peak for NO_x and potential temperature θ with the vertical
160 wind speed, respectively, for three segments on June 6. For all three segments shown here the covariance for NO_x and vertical
windspeed is clearly identifiable. The covariance peak for θ and the vertical windspeed can only be determined for two of these
segments (middle and right panel). However, particularly for NO_x, the identified lag times match quite well. As we expect the
lag time not to vary throughout one flight (its variation is primarily associated with alignment of different computer clocks
and not variation in the transit time to the detection point), we correct all segments with the median lag time of the identified
165 segments. We show an example co-spectrum for the NO_x flux and the heat flux in Figure S3 of the Supplement, for three
segments on June 6 corresponding to Figure S2. The Nyquist frequency which is equal to half the sampling frequency is shown
as black dotted lines. We were able to capture most eddies due to the high sampling frequency of 5 Hz. Similar to the lag-
covariance however, we observe difficulties for some of the segments. We explicitly chose positive and negative examples of
lag-covariance and co-spectra plots here to underline the strength, but also the limitation of our data quality which varies from
170 segment to segment and is dependent on various factors, including the instrumental performance, meteorological conditions,
the relative aircraft position within the boundary layer, the aircraft speed, the segment length, changes in altitude and the roll
angle of the aircraft. A detailed error analysis and discussion can be found in Zhu et al. (2023).

The overall uncertainty of the calculated NO_x flux is composed of the uncertainty of the measurement of the NO_x concentration and the vertical wind speed. We find that the NO_x median and average values are dominated by the atmospheric variability and not the measurement uncertainties. The observed atmospheric variability of NO_x is in the order of 30 % (1σ) which is around 4 times higher than the instrumental precision of $< 7 \%$ (1σ). Additional uncertainty is associated with the presented method of performing the wavelet transformation, including random and systematic errors (Lenschow et al., 1994; Mann and Lenschow, 1994; Wolfe et al., 2015; Vaughan et al., 2021). A detailed error analysis for these observations is provided in Zhu et al. (2023).

180 2.5 Vertical Divergence

Vertical flux divergence describes the effect that a flux measured at a certain altitude can differ from the surface flux caused for example through chemistry conversions, entrainment from above or horizontal advection (Wolfe et al., 2018; Vaughan et al., 2021). The characterization of the vertical divergence can be performed by measurements of a vertical profile over a homogeneous surface. Several race tracks stacked at multiple heights were conducted over Los Angeles during RECAP-CA, but none fulfilled the criteria for performing flux calculations as described in Section 2.4 (e.g. roll angle or segment length). A different approach is described in Wolfe et al. (2018) and Zhu et al. (2023) which investigates the vertical profile of the calculated NO_x fluxes, normalized to the boundary layer height over a homogeneous surface. In contrast to the San Joaquin Valley considered in Zhu et al. (2023), the measurements over Los Angeles are not homogeneous, neither in space nor in time, due to a high variety of emission sources and a diurnal cycle affected e.g. by rush hour traffic. In Figure S4 of the Supplement we show the calculated NO_x flux across Los Angeles versus the dimensionless altitude z/z_i , where z is the radar altitude of the research aircraft and z_i the boundary layer height. Figure S5 presents the distribution of these data points as a density plot. The data points exhibit a decreasing trend (green) with altitude pointing towards the effect of vertical divergence, but show a low statistical significance with an R^2 of only 6 %, likely due to the source heterogeneity, both space- and time-wise. In order to investigate the influence of vertical divergence, we compare an analysis with a correction of the fluxes using the linear fit of the NO_x flux (F_z) and the dimensionless altitude (z/z_i) as shown in Figure S4 to our analysis assuming the divergence is zero, which we will refer to as 'sensitivity study' in the following. We use a correction factor as presented in Eq. (15) in Wolfe et al. (2018). The uncertainty of this correction is dominated by the uncertainty in the fitted line, which arises from describing F_z vs z/z_i with a linear function as presented in Figure S4. The resulting surface flux F_0 can then be calculated as shown in Equation (7), with the measured flux F_z at the altitude z/z_i , the slope m of the linear fit and its y-intercept c .

$$200 \quad F_0 = \frac{F_z}{1 + \frac{m}{c} * z/z_i} \quad (7)$$

We show the fluxes adjusted for this estimate of the vertical divergence versus the dimensionless altitude in Figure S6 of the Supplement. Data points which are located close to the linear fit can be corrected quite accurately. However, corrections for data points which are located further away from the fit, and particularly those measured close to the boundary layer height, are highly uncertain. As the slope is negative, and the absolute values for slope and y-intercept are almost equal, the denominator

205 in Equation (7) gets extremely small close to the BLH and the correction correspondingly large. Karl et al. (2013) also suggests that fluxes can get uncertain close to the boundary layer height due to entrainment to the free troposphere. Thus, for the sensitivity study, we omit data points within the upper 20 % of the boundary layer ($z/z_i \geq 0.8$), as a trade-off between high uncertainties close to the top of the PBL and the associated data loss. Additionally, the upper 20% of the boundary layer were found to be most likely influenced by entrainment (Druihet and Durand, 1984; Stull, 1988). The corrected fluxes filtered by
 210 the upper 20% of BL are shown in Figure S7.

2.6 Footprint calculations

In order to map emissions, we performed footprint calculations which help to identify the areas over which the associated sources and sinks influence the observed fluxes (Vesala et al., 2008). We used the footprint model KL04-2D, proposed by Kljun et al. (2004), and further developed by Metzger et al. (2012) to include the impact of cross winds. The KL04 model was
 215 developed from the 3D backward Lagrangian model KL02 (Kljun et al., 2002). This model was previously applied by Vaughan et al. (2021).

We subdivided the area of observations into a $500 \text{ m} \times 500 \text{ m}$ spatial grid and calculated an average of all data points located in one grid box, separately for each segment. We then performed the footprint calculation for each grid box of each segment, approximately 5,000 footprints for the entire campaign. The footprint calculation is dependent on the wind direction [°], the
 220 crosswind fluctuations (standard deviation of the horizontal wind speed) [m/s], the vertical wind fluctuations (standard deviation of the vertical wind speed) [m/s], the friction velocity [m/s], the roughness length [m], the altitude of the measurement above ground level [m] and the height of the planetary boundary layer [m]. Please find details on the acquisition of the meteorological inputs in Section 2.2. The roughness length z_0 is a measure of the surface properties, which we adapted from Burian et al. (2002) and from the World Meteorological Organization (2018) based on the land cover use for Los Angeles. We
 225 first generated footprints using the roughness length from the High-Resolution Rapid Refresh (HRRR) model by the National Oceanic and Atmospheric Administration (NOAA, 2021). Based on the dominant land cover type in each footprint, we then applied the roughness length according to Burian et al. (2002) and the World Meteorological Organization (2018). The land use data set was obtained from the Multi-Resolution Land Characteristics Consortium (MRLC, 2019). The friction velocity u^* is a measure for the shear stress and can be approximated via the logarithmic wind profile as shown in Eq. (8), where u is
 230 the horizontal wind speed, k the Karman constant equaling 0.41, z the altitude above ground level and z_0 the roughness length (Weber, 1999).

$$u^* = u \times k \times \ln\left(\frac{z}{z_0}\right)^{-1} \quad (8)$$

The model output is a spatial grid of the fractional contribution to each footprint normalized to a value of unity. We focused on the 90 % footprint influences and assigned the measured NO_x flux to the NO_x flux of each grid box in the 90 % footprints.
 235 We then overlaid all footprint grids separately for weekends and for weekdays and calculated a value for the NO_x flux for each grid box as the weighted average.

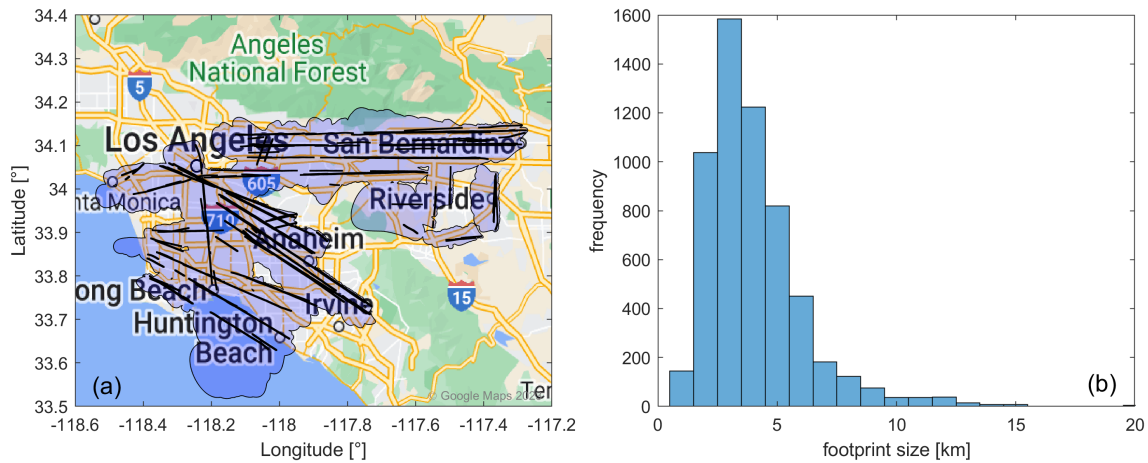


Figure 3. (a) Overview of the 90 % footprint influences for the flight campaign over Los Angeles. © Google Maps 2023. (b) Frequency distribution of the 90 % footprint size which describes the distance perpendicular to the flight track.

Figure 3a presents the 90 % contours of all segments over Los Angeles in blue and the according flight paths in black. The majority of the 90 % footprints captured air masses from a distance of ~ 3 km (perpendicular to the flight track) as shown in the histogram of footprint size in Figure 3b. We observed individual footprints with a size of up to 22.5 km, for example for
 240 19 June around Huntington Beach which were accompanied by high horizontal wind speeds ($\sim 5 \text{ m s}^{-1}$) and a flight altitude ($\sim 380 \text{ m}$) in the upper part of the boundary layer (BLH of $\sim 410 \text{ m}$). This is in line with the findings by Kljun et al. (2004), demonstrating the impact of the receptor height (Fig. 1 in Kljun et al. (2004)). The smallest footprint with 500 m was observed on 12 June, characterized by a small value for the horizontal wind speed with $\sim 0.3 \text{ m s}^{-1}$. The flight took place roughly in the middle of the boundary layer at an altitude of $\sim 315 \text{ m}$ with a BLH of $\sim 500 \text{ m}$.

245 The influence of the horizontal wind speed on the footprint analysis is also highlighted in Figure 4. The two panels present selected flight segments colored by the NO_x flux in geographic proximity over the San Bernardino valley on 6 June (Figure 4a) and on 12 June (Figure 4b). Both days were weekend days and we expect similar NO_x emissions. However, the calculated NO_x flux for the displayed segments was on average $0.08 \pm 0.09 \text{ mg N m}^{-2} \text{ h}^{-1}$ for 6 June and $0.53 \pm 0.34 \text{ mg N m}^{-2} \text{ h}^{-1}$ for 12 June. At the same time, the footprint size for these segments, represented by the black lines, was more than 4 times larger
 250 for 6 June with an average of $7.1 \pm 2.5 \text{ km}$, than for 12 June with an average of $1.9 \pm 1.0 \text{ km}$. The measured air on 12 June originated from above the highways in the San Bernardino valley. In contrast, on 6 June we also captured air from adjacent, less NO_x sources, such as residential areas, diluting the NO_x polluted air from above the highways and leading to lower NO_x fluxes. While all inputs for the footprint model were roughly similar (e.g. radar altitude 383 m (June 6) and 349 m (June 12); BLH 637 m (June 6) and 600 m (June 12)), the horizontal wind speed was significantly higher on 6 June with an average
 255 of $8.2 \pm 1.2 \text{ m s}^{-1}$ than on June 12 where the average was $2.5 \pm 1.0 \text{ m s}^{-1}$. This example also underlines the importance of footprint calculations in the interpretation of the observed fluxes.

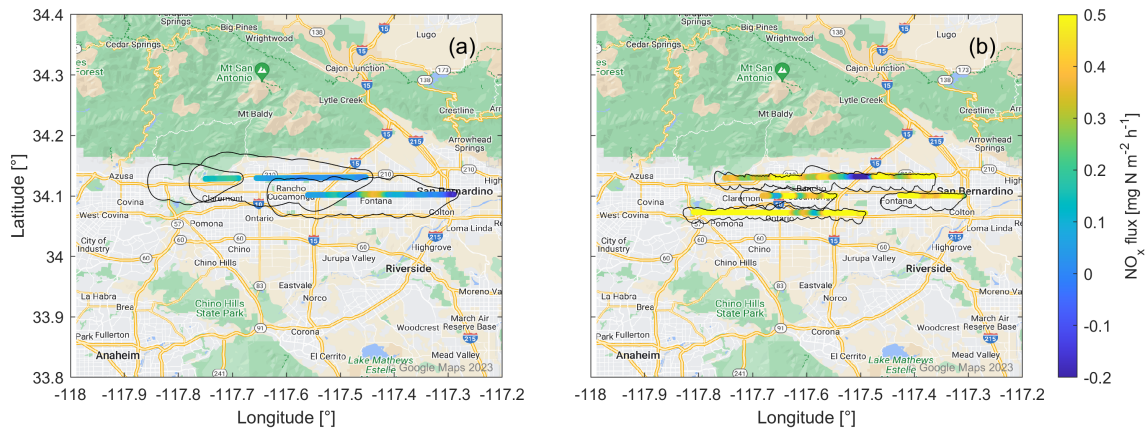


Figure 4. Flight segments colored by the NO_x flux in geographic proximity on two weekend days, (a) 6 June and (b) 12 June, with different footprint size. The black lines represent the contour of the 90% footprints. © Google Maps 2023.

2.7 Emission inventory

The California Air Resources Board (CARB) provides an emission inventory for Los Angeles with a 1 hour temporal resolution and a $4 \text{ km} \times 4 \text{ km}$ spatial resolution over 12 vertical layers. The emission inventory is assembled from several sub-models accounting for different emission source categories. These are on-road vehicle emissions, aircraft emission and all other emissions, including for example shipping and port emissions. Mobile emissions are obtained via the ESTA (Emissions Spatial and Temporal Allocator) model (CARB, 2019). Emissions from vehicles, including passenger cars, buses and heavy-duty trucks, are estimated via the EMFAC (EMission FACTor) model based on vehicle registrations and emission rate data for different vehicle types (CARB, 2021, 2022a). In combination with spatial information and temporal data, such as diurnal profiles and day-of-week dependence, the on-road emission inventory can be created via the ESTA model (CARB, 2019). The GATE (Grid-
 260
 265
 270
 275

ded Aircraft Trajectory Emissions) model analogously provides spatially and temporally resolved aircraft emissions (CARB, 2017). Emissions from shipping and port activities, as well as additional point or area sources, are modeled with the SMOKE (Sparse Matrix Operator Kernel Emissions) model (CEMPD, 2022). We are presenting a comparison of the NO_x fluxes calculated from the RECAP-CA campaign measurements with the 2020 CARB emission inventory for Los Angeles, which is a baseline inventory and therefore does not include any effects related to the COVID-19 (coronavirus disease 2019) economic and social upheaval. For each flight day of the 2021 campaign, we include the according day of the week of the emission inventory in 2020. As 2020 was a leap year, the day of year of each considered flight is shifted by two from the 2020 calendar (e.g. Tuesday, 1 June, was the 152nd day of 2021 for which we consider Tuesday, 2 June, the 154th day of 2020, from the emission inventory). We combined the $500 \text{ m} \times 500 \text{ m}$ spatial resolution of the RECAP-CA NO_x fluxes to the $4 \text{ km} \times 4 \text{ km}$ CARB grid for this comparison.

3 Results and Discussion

3.1 NO_x emissions over Los Angeles

NO_x mixing ratios and NO_x fluxes over Los Angeles are separated into four different geographical regions, as shown in Figure 1b. We analyze the effects of temperature and the planetary boundary layer height, as well as differences between weekend and weekday data. Figure 5 shows the temperature for the different sections, measured on the research aircraft (380 ± 63 m altitude). Lowest temperatures were observed in the coastal section with a median value of 17°C . Temperatures measured over Santa Ana and Downtown were slightly higher with median values around 19°C . Further inland, observed temperatures were highest with a median value of 24°C . Differences between the four sections were also observed regarding the boundary layer height (BLH) as presented in Figure 5b. The lowest BLH was found for the coastal section with a median value of 470 m, followed by Santa Ana with 490 m and a median value of 540 m for Downtown. The BLH in the San Bernardino valley was highest with a median value of 590 m. Figure 5c shows NO_x mixing ratios and Figure 5d shows the corresponding fluxes over Los Angeles, separated into the geographical sections and into weekdays and weekends. Neither NO_x mixing ratios nor NO_x fluxes were found to be temperature dependent (see Figure S8).

Median mixing ratios were highest in Downtown with 6.5 ppbv on weekdays and 3.4 ppbv on weekends. In the San Bernardino valley, median concentrations were 5.8 ppbv and 4.1 ppbv on weekdays and weekends, respectively. The observed levels of NO_x reductions from weekdays to weekends are consistent with previous results based on ground-based measurements across Los Angeles, which, for example, we have investigated in Nussbaumer and Cohen (2020). The median measured fluxes in Downtown Los Angeles were 0.27 and 0.12 $\text{mg N m}^{-2} \text{h}^{-1}$, respectively for weekdays and weekends. In the San Bernardino valley the median fluxes were 0.31 $\text{mg N m}^{-2} \text{h}^{-1}$ on weekdays and 0.15 $\text{mg N m}^{-2} \text{h}^{-1}$ on weekends. In all of these locations weekend emissions decreased by 50 - 60 % from weekday values.

Mixing ratios were lower near the coast. Median NO_x mixing ratios were similar for the coastal section and Santa Ana with 2.8–3.0 ppbv on weekdays. The weekend values were smaller with 2.0–2.3 ppbv. However, no significant differences could be observed between weekday and weekend fluxes in these regions. Much of the coastal region is over water and the median values of fluxes are near zero on both weekdays and weekends and approximately 0.1 $\text{mg N m}^{-2} \text{h}^{-1}$ on both weekdays and weekends in the Santa Ana region.

While NO_x concentrations were observed to be highest over Downtown Los Angeles, NO_x fluxes were found to be highest in the San Bernardino valley. This effect could be partly caused by the observed differences in the boundary layer height. While highest emissions occurred in the San Bernardino valley, the increased planetary BLH (as shown in Figure 5b), should lead to a $\sim 15\%$ lower mixing ratio. The differences in concentrations are likely also due to chemistry and advection.

Using the highway information by the California Department of Transportation (2015), we separated NO_x fluxes into emissions from highway and non-highway grid cells. A $500\text{ m} \times 500\text{ m}$ grid cell is considered a highway emission when it is crossed by a highway. We present the resulting emission grid in Figure S9 of the Supplement. For weekdays, NO_x fluxes from highway grid cells were on average 0.27 ± 0.48 $\text{mg N m}^{-2} \text{h}^{-1}$, approximately 25 % higher than NO_x fluxes from non-highway grid cells with an average of 0.22 ± 0.42 $\text{mg N m}^{-2} \text{h}^{-1}$. Weekend NO_x fluxes from highways were on average

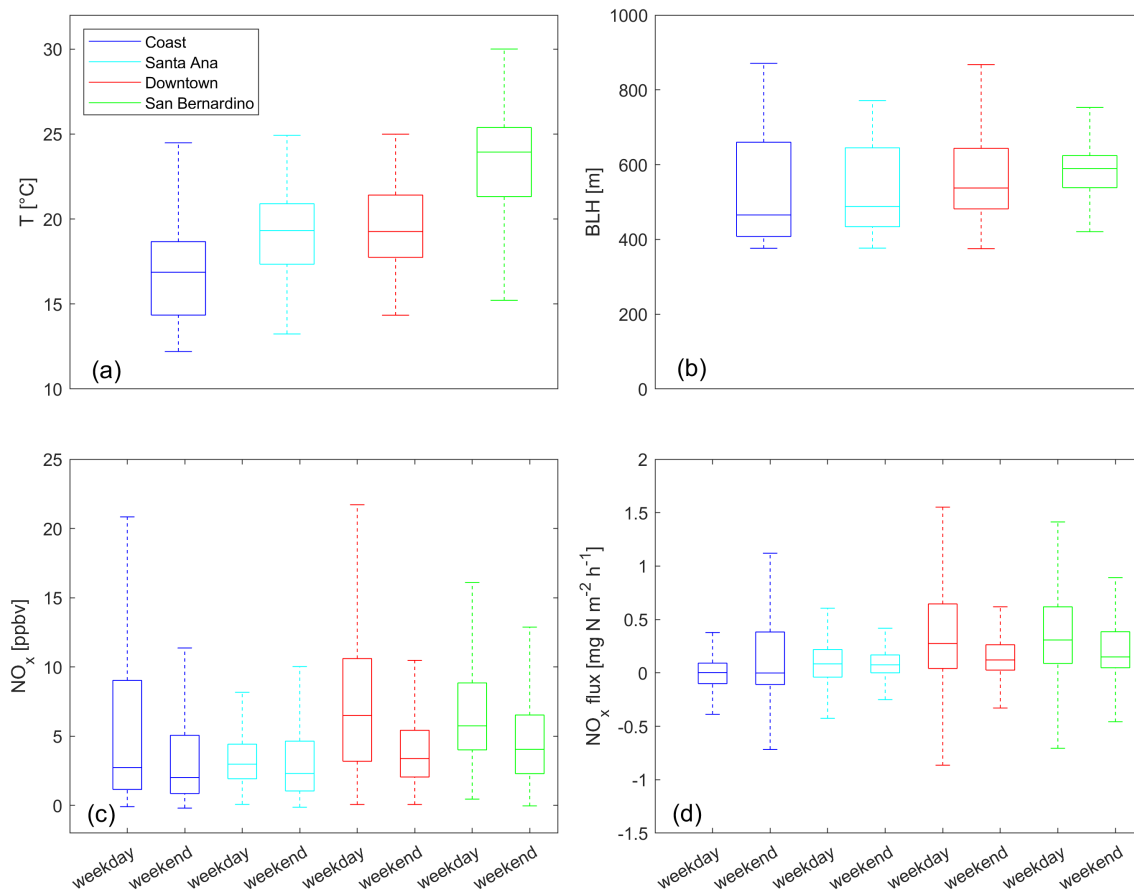


Figure 5. Boxplots for (a) the temperature, (b) the boundary layer height, (c) NO_x concentrations and (d) NO_x fluxes subdivided into four geographical sections according to Figure 1b (same color-code) and into weekday and weekend data. Blue colors represent the Coast, cyan colors the Santa Ana region, red colors Downtown Los Angeles and green colors the San Bernardino valley. Please note that outliers are not shown.

310 $0.19 \pm 0.31 \text{ mg N m}^{-2} \text{ h}^{-1}$. Weekend NO_x emissions from non-highway areas were $0.15 \pm 0.32 \text{ mg N m}^{-2} \text{ h}^{-1}$. Note the large 1σ standard deviations, indicating the large variability of the fluxes. The median values were lower compared to the mean values (0.18 and $0.10 \text{ mg N m}^{-2} \text{ h}^{-1}$ for highway and non-highway, respectively, on weekdays and 0.09 and $0.13 \text{ mg N m}^{-2} \text{ h}^{-1}$ for highway and non-highway, respectively, on weekends), but showed a similar qualitative result with higher emissions from highway compared to non-highway areas.

315 3.2 Comparison to the emission inventory

The comparison between the emission inventory and the calculated NO_x fluxes is shown in Figure 6. We present the weekday data here and show the weekend data in Figure S10 of the Supplement. This Figure presents measured NO_x fluxes, which are

not corrected for vertical divergence. We present the results of the sensitivity study (as described in Section (2.5)) applying a correction according to the linear fit presented in Figure S4 and discuss the implications of this correction at the end of this Section. Panel (a) shows the RECAP-CA NO_x fluxes at $4 \text{ km} \times 4 \text{ km}$, panel (b) presents the CARB emission inventory and in panel (c) we show the difference between the CARB and the RECAP-CA data. Red colors indicate higher fluxes from the emission inventory and blue colors show higher fluxes from the RECAP-CA airborne measurements. As expected from the results presented in Section 3.1 the highest NO_x fluxes were observed in the San Bernardino valley which is characterized by several heavily trafficked highways and warehouses that cause dense diesel truck traffic (Los Angeles Times, 2023). Elevated NO_x emission also occurred in the region around Downtown Los Angeles. The average weekend RECAP-CA NO_x fluxes (Figure S10a) showed a similar emission distribution over Los Angeles compared to the weekday data, but with smaller values. This is in line with the findings presented in Section 3.1.

Figure 6b shows average weekday NO_x fluxes as predicted by the CARB emission inventory. The large NO_x flux in proximity to the coast ($\sim 34.0^\circ \text{ N}$, 118.4° W) with a value close to $3.5 \text{ mg N m}^{-2} \text{ h}^{-1}$ was associated with aircraft emissions, as well as ground handling equipment and vehicle traffic, from and around Los Angeles International Airport (LAX). Additionally, emissions from aircraft not only at the surface but also at elevated altitudes could contribute to the observed value. We show the NO_x fluxes as predicted by CARB separated into (a) on-road emissions, (b) aircraft emissions, (c) area sources (e.g. residential heating or cooking emissions which accumulate over a larger area (CARB, 2023)) and (d) emissions from ocean going vessels in Figure S11 of the Supplement. Aircraft NO_x emissions can also be observed in the San Bernardino valley ($\sim 34.1^\circ \text{ N}$, 117.6° W) from Ontario International Airport which is illustrated in Figure S11b. High NO_x fluxes in this area were also associated with on-road emissions, shown in Figure S11a. The Downtown Los Angeles area ($\sim 34.0^\circ \text{ N}$, 118.2° W) also showed high fluxes which originated from on-road and area sources. Elevated NO_x fluxes around Long Beach ($\sim 33.8^\circ \text{ N}$, 118.2° W) were associated with shipping and port emissions. Average weekend NO_x fluxes predicted by the emission inventory are presented in Figure S11b which showed a similar qualitative distribution compared to the weekday data, but were generally lower. Figure 6c presents the difference between the NO_x fluxes from the RECAP-CA campaign and the CARB emission inventory. Blue colors represent higher values for the RECAP-CA campaign compared to the emission inventory. Red colors indicate higher fluxes from the emission inventory. In most places, the NO_x fluxes predicted by the emission inventory were higher compared to the values from the RECAP-CA campaign. This difference was particularly pronounced in the area around Downtown Los Angeles and along the coast. Due to lively air traffic, the research aircraft could not approach the airport closely and the footprints only covered a minor area of LAX airport. As a result the differences in the vicinity of the airport should not be interpreted as meaningful. NO_x fluxes around Downtown Los Angeles are dominated by area sources and on-road emissions.

We observed higher NO_x fluxes during the RECAP-CA campaign compared to the emission inventory in the San Bernardino valley. A possible explanation could be the accumulation of distribution and fulfillment centers which are accessible to delivery trucks via multiple highways in this area (Schorung and Lecourt, 2021; Los Angeles Times, 2023). Over the past two decades net sales via distribution centers have grown exponentially (Statista, 2022a). In the U.S., the number of delivered orders by the online retailer Amazon has increased by nearly a factor of 6 between 2018 and 2020 (Statista, 2022b). NO_x emissions in

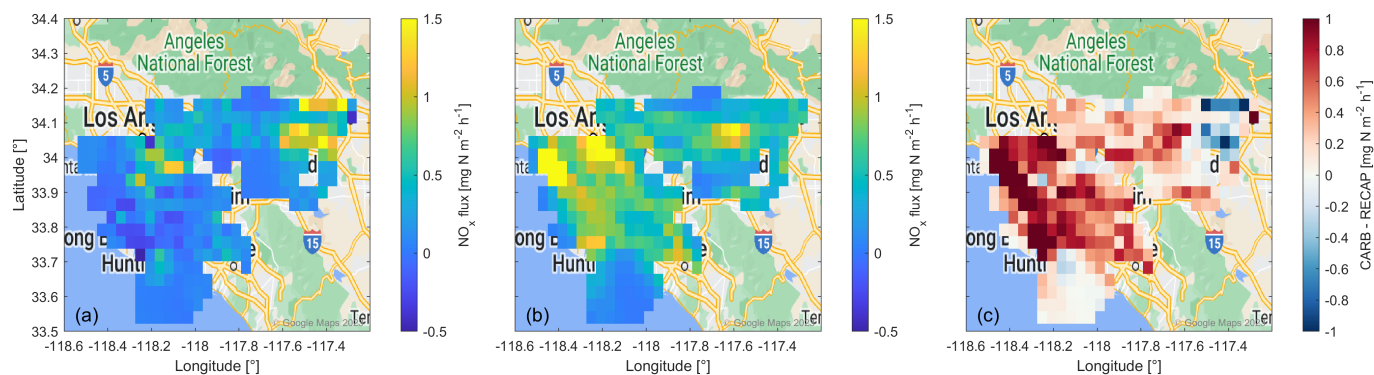


Figure 6. Weekday averages of NO_x emissions across Los Angeles with a 4 km × 4 km spatial resolution (a) during the RECAP-CA campaign, (b) from the CARB emission inventory and (c) the difference between CARB and RECAP-CA NO_x fluxes. © Google Maps 2023.

proximity to warehouses have likely increased to a similar extent in recent years which might not yet be incorporated in the CARB 2020 emission inventory. Additional research is needed to examine more details of these differences and connect them to specific processes in the inventory and observations.

In Figure S12 and S13 of the Supplement we show the NO_x fluxes corrected for vertical divergence as presented in Section 2.5 in comparison to the CARB emission inventory for weekdays and weekends, respectively. The emission features shown in Figure 6 for the RECAP-CA campaign are more pronounced after applying the factor for vertical correction. High emissions are observed over Downtown Los Angeles and the inland highways in San Bernardino, while the coastal region and Santa Ana show lower, and even negative fluxes. As a result, CARB emissions remain dominant over RECAP-CA fluxes in the coastal region, but are lower around Downtown Los Angeles and in San Bernardino. The median values of the corrected fluxes are around a factor of 3 higher compared to the non-corrected fluxes. The interquartile range increases by even more as a result of the large scatter induced by the correction (compare Figures S6 and S7). We do not correct the fluxes for vertical divergence as our data set does not provide significant or unambiguous indication for its occurrence and extent. This is likely an outcome of the source heterogeneity experienced across Los Angeles as most emissions are highly variable in time and space. In previous studies, the vertical divergence has been successfully characterized via the correlation of the flux and the dimensionless altitude over homogeneous surfaces, which is not applicable to Los Angeles. Instead, carefully planned stacked race track flights could provide insights into vertical flux divergence. This sensitivity analysis emphasizes how important the characterization of the vertical flux divergence is and should be subject to future studies.

370 4 Conclusions

In this study, we have investigated NO_x fluxes via wavelet analysis, based on airborne observations of NO_x concentrations and the vertical wind speed during the research aircraft campaign RECAP-CA which took place in June 2021 over Los Angeles. We identified NO_x concentrations to be highest over Downtown Los Angeles, while we found highest NO_x fluxes in the San

Bernardino valley where a high planetary BLH induced a higher dilution of the emitted NO_x . Both NO_x concentrations and
375 NO_x fluxes revealed a weekend effect with higher values on weekdays due to more commuter traffic and more diesel trucks
on roads, which was most pronounced over Downtown Los Angeles and the San Bernardino valley. Footprint calculations
revealed that the distance of the 90 % influence was on average 4 km upwind, whereby the horizontal wind speed played a
dominant role in the footprint size. NO_x emissions predicted by the California Air Resources Board (CARB) 2020 were in the
same order of magnitude, but on average higher compared to the RECAP-CA NO_x fluxes. Spatially, the emission inventory
380 overestimated the fluxes in coastal proximity and over Downtown Los Angeles, which could be due to COVID-19 related
reductions, such as a shift to more remote work and less commuter traffic, general emission reductions not yet captured by the
emission inventory, or misallocation of emission sources in the inventory. In contrast, the emission inventory underestimated
the NO_x fluxes over the Eastern part of the San Bernardino valley where an increased activity of trucks going to and from
warehouses due to the exponential growth of online retailers, such as Amazon, lead to higher NO_x emissions in recent years. A
385 single uniform correction for vertical divergence could locally lead to improved agreement in this part of the domain, but would
at the same time increase the difference in other parts of the studied area. Being an important tool in air quality regulation, we
encourage further investigation of the accuracy of local emission inventories with observations from aircraft, towers or dense
networks. For flux measurements from aircraft or towers, a particular focus on improving vertical divergence characterization,
in order to provide accurate emission predictions would be especially beneficial.

390 *Data availability.* Data measured during the flight campaign, computed fluxes and footprints are available at <https://doi.org/10.5281/zenodo.8199013> (Nussbaumer et al., 2023). Additional files, e.g. in different resolutions, are available from the corresponding authors upon request.

Author contributions. CMN analyzed the data with contributions from BKP, QZ and EYP. CMN wrote the manuscript. All authors contributed to designing the study and proofreading the manuscript.

Competing interests. At least one of the (co-)authors is a member of the editorial board of Atmospheric Chemistry and Physics.

395 *Acknowledgements.* We acknowledge Horst Fischer and Lenard Röder for valuable discussions and proofreading of this manuscript. The RECAP-CA aircraft campaign was funded by the California Air Resources Board (20RD003 and 20AQP012) and the South Coast Air Quality Management District (#20327). The wavelet software was provided by C. Torrence and G. Compo, and is available at URL: <http://paos.colorado.edu/research/wavelets/>. Plots including Google Maps data were created with a matlab function by Bar-Yehuda, Z. (2022). This work was supported by the Max Planck Graduate Center with the Johannes Gutenberg-Universität Mainz (MPGC).

400 References

- American Lung Association: Most Polluted Cities, <https://www.lung.org/research/sota/city-rankings/most-polluted-cities>, accessed on 2022-04-08, 2022.
- Bar-Yehuda, Z.: zoharby plot google map, https://github.com/zoharby/plot_google_map, retrieved on 2022-07-11, 2022.
- Boningari, T. and Smirniotis, P. G.: Impact of nitrogen oxides on the environment and human health: Mn-based materials for the NO_x abatement, *Current Opinion in Chemical Engineering*, 13, 133–141, <https://doi.org/10.1016/j.coche.2016.09.004>, 2016.
- 405 Burian, S. J., Brown, M. J., and Velugubantla, S. P.: Roughness length and displacement height derived from building databases, <https://www.osti.gov/biblio/976101>, 2002.
- California Department of Transportation: State Highways (Segments), California, 2015, available at <https://searchworks.stanford.edu/view/x453kn9742>, accessed on 2022-07-15, 2015.
- 410 CARB: GATE Basic Introduction, https://github.com/mmb-carb/GATE_Documentation/blob/master/docs/BASIC_INTRO.md, accessed on 2022-05-30, 2017.
- CARB: ESTA Basic Introduction, https://github.com/mmb-carb/ESTA_Documentation/blob/master/docs/BASIC_INTRO.md, accessed on 2022-05-30, 2019.
- CARB: EMFAC2021 Volume III Technical Document, Tech. rep., Mobile Source Analysis Branch Air Quality Planning and Science Division, https://ww2.arb.ca.gov/sites/default/files/2021-08/emfac2021_technical_documentation_april2021.pdf?utm_medium=email&utm_source=govdelivery, accessed on 2022-05-31, 2021.
- 415 CARB: Welcome to EMFAC, <https://arb.ca.gov/emfac/>, accessed on 2022-05-31, 2022a.
- CARB: Nitrogen Dioxide and Health, <https://ww2.arb.ca.gov/resources/nitrogen-dioxide-and-health>, accessed on 2022-04-07, 2022b.
- CARB: Criteria Pollutant Emission Inventory Data, <https://ww2.arb.ca.gov/criteria-pollutant-emission-inventory-data>, accessed on 2023-07-17, 2023.
- 420 CEMPD: SMOKE, <https://github.com/CEMPD/SMOKE/>, center for Environmental Modeling for Policy Development, accessed on 2022-05-31, 2022.
- Conley, S., Faloon, I., Miller, G., Lenschow, D., Blomquist, B., and Bandy, A.: Closing the dimethyl sulfide budget in the tropical marine boundary layer during the Pacific Atmospheric Sulfur Experiment, *Atmospheric Chemistry and Physics*, 9, 8745–8756, <https://doi.org/10.5194/acp-9-8745-2009>, 2009.
- 425 Day, D., Wooldridge, P., Dillon, M., Thornton, J., and Cohen, R.: A thermal dissociation laser-induced fluorescence instrument for in situ detection of NO₂, peroxy nitrates, alkyl nitrates, and HNO₃, *Journal of Geophysical Research: Atmospheres*, 107, ACH-4, <https://doi.org/10.1029/2001JD000779>, 2002.
- Delmas, R., Serça, D., and Jambert, C.: Global inventory of NO_x sources, *Nutrient cycling in agroecosystems*, 48, 51–60, 1997.
- 430 Desjardins, R. L., Worth, D. E., MacPherson, I., Mauder, M., and Bange, J.: Aircraft-Based Flux Density Measurements. In: *Springer Handbook of Atmospheric Measurements*, pp. 1305–1330, Springer International Publishing, Cham, https://doi.org/10.1007/978-3-030-52171-4_48, 2021.
- Druilhet, A. and Durand, P.: Etude de la couche limite convective sahélienne en présence de brumes sèches (Expérience ECLATS), *Boundary-layer meteorology*, 28, 51–77, <https://doi.org/10.1007/BF00119456>, 1984.
- 435 EPA: Overview of the Clean Air Act and Air Pollution, <https://www.epa.gov/clean-air-act-overview>, accessed on 2022-04-07, 2022a.

- EPA: Air Data - Ozone Exceedances, <https://www.epa.gov/outdoor-air-quality-data/air-data-ozone-exceedances>, accessed on 2022-04-07, 2022b.
- EPA: California Nonattainment/Maintenance Status for Each County by Year for All Criteria Pollutants, https://www3.epa.gov/airquality/greenbook/anayo_ca.html, accessed on 2022-04-08, 2022c.
- 440 Fujita, E. M., Campbell, D. E., Stockwell, W. R., and Lawson, D. R.: Past and future ozone trends in California's South Coast Air Basin: Reconciliation of ambient measurements with past and projected emission inventories, *Journal of the Air & Waste Management Association*, 63, 54–69, <https://doi.org/10.1080/10962247.2012.735211>, 2013.
- Gu, D., Guenther, A. B., Shilling, J. E., Yu, H., Huang, M., Zhao, C., Yang, Q., Martin, S. T., Artaxo, P., Kim, S., Seco, R., Stavrou, T., Longo, K. M., Tóta, J., de Souza, R. A. F., Vega, O., Liu, Y., Shrivastava, M., Alves, E. G., Santos, F. C., Leng, G., and
445 Hu, Z.: Airborne observations reveal elevational gradient in tropical forest isoprene emissions, *Nature communications*, 8, 15 541, <https://doi.org/10.1038/ncomms15541>, 2017.
- Hegg, D. A., Covert, D. S., Jonsson, H., and Covert, P. A.: Determination of the transmission efficiency of an aircraft aerosol inlet, *Aerosol science and technology*, 39, 966–971, <https://doi.org/10.1080/02786820500377814>, 2005.
- Karl, T., Apel, E., Hodzic, A., Riemer, D., Blake, D., and Wiedinmyer, C.: Emissions of volatile organic compounds inferred from airborne
450 flux measurements over a megacity, *Atmospheric Chemistry and Physics*, 9, 271–285, <https://doi.org/10.5194/acp-9-271-2009>, 2009.
- Karl, T., Misztal, P., Jonsson, H., Shertz, S., Goldstein, A., and Guenther, A.: Airborne flux measurements of BVOCs above Californian oak forests: Experimental investigation of surface and entrainment fluxes, OH densities, and Damköhler numbers, *Journal of the atmospheric sciences*, 70, 3277–3287, <https://doi.org/10.1175/JAS-D-13-054.1>, 2013.
- Kaser, L., Karl, T., Yuan, B., Mauldin III, R., Cantrell, C., Guenther, A. B., Patton, E., Weinheimer, A. J., Knote, C., Orlando, J., Emmons,
455 L., Apel, E., Hornbrook, R., Shertz, S., Ullmann, K., Hall, S., Graus, M., de Gouw, J., Zhou, X., and Ye, C.: Chemistry-turbulence interactions and mesoscale variability influence the cleansing efficiency of the atmosphere, *Geophysical Research Letters*, 42, 10–894, <https://doi.org/10.1002/2015GL066641>, 2015.
- Kljun, N., Rotach, M., and Schmid, H.: A three-dimensional backward Lagrangian footprint model for a wide range of boundary-layer stratifications, *Boundary-Layer Meteorology*, 103, 205–226, <https://doi.org/10.1023/A:1014556300021>, 2002.
- 460 Kljun, N., Calanca, P., Rotach, M., and Schmid, H.: A simple parameterisation for flux footprint predictions, *Boundary-Layer Meteorology*, 112, 503–523, <https://doi.org/10.1023/B:BOUN.0000030653.71031.96>, 2004.
- Lenschow, D., Mann, J., and Kristensen, L.: How long is long enough when measuring fluxes and other turbulence statistics?, *Journal of Atmospheric and Oceanic Technology*, 11, 661–673, [https://doi.org/10.1175/1520-0426\(1994\)011<0661:HLILEW>2.0.CO;2](https://doi.org/10.1175/1520-0426(1994)011<0661:HLILEW>2.0.CO;2), 1994.
- Los Angeles Times: Warehouse boom transformed Inland Empire. Are jobs worth the environmental degradation?, https://www.latimes.com/california/story/2023-02-05/warehouses-big-rigs-fill-inland-empire-streets?utm_id=85748&sfmc_id=1882085, accessed on 2023-03-06,
465 2023.
- Mann, J. and Lenschow, D. H.: Errors in airborne flux measurements, *Journal of Geophysical Research: Atmospheres*, 99, 14 519–14 526, <https://doi.org/10.1029/94JD00737>, 1994.
- Metzger, S., Junkermann, W., Mauder, M., Beyrich, F., Butterbach-Bahl, K., Schmid, H. P., and Foken, T.: Eddy-covariance flux measure-
470 ments with a weight-shift microlight aircraft, *Atmospheric Measurement Techniques*, 5, 1699–1717, <https://doi.org/10.5194/amt-5-1699-2012>, 2012.

- Metzger, S., Junkermann, W., Mauder, M., Butterbach-Bahl, K., Trancón y Widemann, B., Neidl, F., Schäfer, K., Wieneke, S., Zheng, X. H., Schmid, H. P., and Foken, T.: Spatially explicit regionalization of airborne flux measurements using environmental response functions, *Biogeosciences*, 10, 2193–2217, <https://doi.org/10.5194/bg-10-2193-2013>, 2013.
- 475 Mills, G., Pleijel, H., Malley, C. S., Sinha, B., Cooper, O. R., Schultz, M. G., Neufeld, H. S., Simpson, D., Sharps, K., Feng, Z., Gerosa, G., Harmens, H., Kobayashi, K., Saxena, P., Paoletti, E., Sinha, V., and Xu, X.: Tropospheric Ozone Assessment Report: Present-day tropospheric ozone distribution and trends relevant to vegetation, *Elementa: Science of the Anthropocene*, 6, <https://doi.org/10.1525/elementa.302>, 2018.
- Misztal, P. K., Karl, T., Weber, R., Jonsson, H. H., Guenther, A. B., and Goldstein, A. H.: Airborne flux measurements of biogenic
480 isoprene over California, *Atmospheric Chemistry and Physics*, 14, 10 631–10 647, <https://doi.org/10.5194/acp-14-10631-2014>, <https://acp.copernicus.org/articles/14/10631/2014/>, 2014.
- MRLC: Multi-Resolution Land Characteristics (MRLC) Consortium - National Land Cover Database, available at <https://www.mrlc.gov/>, accessed on 2022-05-02, 2019.
- NOAA: The High-Resolution Rapid Refresh (HRRR), <https://rapidrefresh.noaa.gov/hrrr/>, accessed on 2022-05-25, 2021.
- 485 Nussbaumer, C. M. and Cohen, R. C.: The Role of Temperature and NO_x in Ozone Trends in the Los Angeles Basin, *Environmental Science & Technology*, 54, 15 652–15 659, <https://doi.org/10.1021/acs.est.0c04910>, 2020.
- Nussbaumer, C. M., Place, B. K., Zhu, Q., Pfannerstill, E. Y., Wooldridge, P., Schulze, B. C., Arata, C., Ward, R., Bucholtz, A., Seinfeld, J. H., Goldstein, A. H., and Cohen, R. C.: Supporting data for: Measurement report: Airborne measurements of NO_x fluxes over Los Angeles during the RECAP-CA 2021 campaign, <https://doi.org/10.5281/zenodo.7786409>, 2023.
- 490 Nuvolone, D., Petri, D., and Voller, F.: The effects of ozone on human health, *Environmental Science and Pollution Research*, 25, 8074–8088, <https://doi.org/10.1007/s11356-017-9239-3>, 2018.
- Pfannerstill, E. Y., Arata, C., Zhu, Q., Schulze, B. C., Woods, R., Seinfeld, J. H., Bucholtz, A., Cohen, R. C., and Goldstein, A. H.: Volatile organic compound fluxes in the San Joaquin Valley – spatial distribution, source attribution, and inventory comparison, *EGU sphere*, 2023, 1–42, <https://doi.org/10.5194/egusphere-2023-723>, 2023.
- 495 Pusede, S. E., Steiner, A. L., and Cohen, R. C.: Temperature and recent trends in the chemistry of continental surface ozone, *Chemical reviews*, 115, 3898–3918, <https://doi.org/10.1021/cr5006815>, 2015.
- Qian, Y., Henneman, L. R., Mulholland, J. A., and Russell, A. G.: Empirical development of ozone isopleths: Applications to Los Angeles, *Environmental Science & Technology Letters*, 6, 294–299, <https://doi.org/10.1021/acs.estlett.9b00160>, 2019.
- Reid, J. S., Jonsson, H. H., Smith, M. H., and Smirnov, A.: Evolution of the vertical profile and flux of large sea-salt particles in a coastal
500 zone, *Journal of Geophysical Research: Atmospheres*, 106, 12 039–12 053, <https://doi.org/10.1029/2000JD900848>, 2001.
- Schaller, C., Göckede, M., and Foken, T.: Flux calculation of short turbulent events – comparison of three methods, *Atmospheric Measurement Techniques*, 10, 869–880, <https://doi.org/10.5194/amt-10-869-2017>, 2017.
- Schörung, M. and Lecourt, T.: Analysis of the spatial logics of Amazon warehouses following a multiscale and temporal approach. For a geography of Amazon’s logistics system in the United States., <https://halshs.archives-ouvertes.fr/halshs-03489397/document>, research report, accessed on 2022-05-31, 2021.
- 505 South Coast Air Quality Management District: Final 2016 air quality management plan, Chapter 2, Tech. rep., South Coast Air Quality Management District, <http://www.aqmd.gov/docs/default-source/clean-air-plans/air-quality-management-plans/2016-air-quality-management-plan/final-2016-aqmp/chapter2.pdf>, accessed on 2022-04-08, 2017.

- Sparks, T. L., Ebben, C. J., Wooldridge, P. J., Lopez-Hilfiker, F. D., Lee, B. H., Thornton, J. A., McDuffie, E. E., Fibiger, D. L.,
510 Brown, S. S., Montzka, D. D., Weinheimer, A. J., Schroder, J. C., Campuzano-Jost, P., Jimenez, J. L., and Cohen, R. C.: Comparison of airborne reactive nitrogen measurements during WINTER, *Journal of Geophysical Research: Atmospheres*, 124, 10483–10502, <https://doi.org/10.1029/2019JD030700>, 2019.
- Statista: Annual net sales revenue of Amazon from 2004 to 2021, <https://www.statista.com/statistics/266282/annual-net-revenue-of-amazoncom/>, accessed on 2022-06-01, 2022a.
- 515 Statista: Number of packages delivered by Amazon Logistics in the United States from 2018 to 2020 (in billion packages)*, <https://www.statista.com/statistics/1178979/amazon-logistics-package-volume-united-states/>, accessed on 2022-06-01, 2022b.
- Stewart, D. R., Saunders, E., Perea, R. A., Fitzgerald, R., Campbell, D. E., and Stockwell, W. R.: Linking air quality and human health effects models: an application to the Los Angeles air basin, *Environmental health insights*, 11, 1178630217737551, <https://doi.org/10.1177/1178630217737551>, 2017.
- 520 Stull, R. B.: An introduction to boundary layer meteorology, vol. 13, Springer Science & Business Media, <https://doi.org/10.1007/978-94-009-3027-8>, 1988.
- Thomas, C. and Foken, T.: Detection of long-term coherent exchange over spruce forest using wavelet analysis, *Theoretical and Applied Climatology*, 80, 91–104, <https://doi.org/10.1007/s00704-004-0093-0>, 2005.
- Thornton, J. A., Wooldridge, P. J., and Cohen, R. C.: Atmospheric NO₂: In situ laser-induced fluorescence detection at parts per trillion
525 mixing ratios, *Analytical Chemistry*, 72, 528–539, <https://doi.org/10.1021/ac9908905>, 2000.
- Torrence, C. and Compo, G. P.: A practical guide to wavelet analysis, *Bulletin of the American Meteorological society*, 79, 61–78, [https://doi.org/10.1175/1520-0477\(1998\)079<0061:APGTWA>2.0.CO;2](https://doi.org/10.1175/1520-0477(1998)079<0061:APGTWA>2.0.CO;2), 1998.
- Vaughan, A. R., Lee, J. D., Misztal, P. K., Metzger, S., Shaw, M. D., Lewis, A. C., Purvis, R. M., Carslaw, D. C., Goldstein, A. H., Hewitt, C. N., Davison, B., and Beevers, Sean D. Karl, T. G.: Spatially resolved flux measurements of NO_x from London suggest significantly
530 higher emissions than predicted by inventories, *Faraday discussions*, 189, 455–472, <https://doi.org/10.1039/c5fd00170f>, 2016.
- Vaughan, A. R., Lee, J. D., Metzger, S., Durden, D., Lewis, A. C., Shaw, M. D., Drysdale, W. S., Purvis, R. M., Davison, B., and Hewitt, C. N.: Spatially and temporally resolved measurements of NO_x fluxes by airborne eddy covariance over Greater London, *Atmospheric Chemistry and Physics*, 21, 15283–15298, <https://doi.org/10.5194/acp-21-15283-2021>, 2021.
- Vesala, T., Kljun, N., Rannik, Ü., Rinne, J., Sogachev, A., Markkanen, T., Sabelfeld, K., Foken, T., and Leclerc, M. Y.: Flux and concentration
535 footprint modelling: State of the art, *Environmental Pollution*, 152, 653–666, <https://doi.org/10.1016/j.envpol.2007.06.070>, 2008.
- Weber, R. O.: Remarks on the definition and estimation of friction velocity, *Boundary-Layer Meteorology*, 93, 197–209, <https://doi.org/10.1023/A:1002043826623>, 1999.
- Wolfe, G. M., Hanisco, T. F., Arkinson, H. L., Bui, T. P., Crouse, J. D., Dean-Day, J., Goldstein, A., Guenther, A., Hall, S. R., Huey, G., Jacob, D. J., Karl, T., Kim, P. S., Liu, X., Marvin, M. R., Mikoviny, T., Misztal, P. K., Nguyen, T. B., Peischl, J., Pollack, I., Ryerson, T., St. Clair,
540 J. M., Teng, A., Travis, K. R., Ullmann, K., Wennberg, P. O., and Wisthaler, A.: Quantifying sources and sinks of reactive gases in the lower atmosphere using airborne flux observations, *Geophysical Research Letters*, 42, 8231–8240, <https://doi.org/10.1002/2015GL065839>, 2015.
- Wolfe, G. M., Kawa, S. R., Hanisco, T. F., Hannun, R. A., Newman, P. A., Swanson, A., Bailey, S., Barrick, J., Thornhill, K. L., Diskin, G., DiGangi, J., Nowak, J. B., Sorenson, C., Bland, G., Yungel, J. K., and Swenson, C. A.: The NASA Carbon Airborne Flux Experiment
545 (CARAFE): instrumentation and methodology, *Atmospheric Measurement Techniques*, 11, 1757–1776, <https://doi.org/10.5194/amt-11-1757-2018>, 2018.

World Meteorological Organization: Flux and concentration footprint modelling: State of the art, 8, World Meteorological Organization, 2018.

550 Yu, H., Guenther, A., Gu, D., Warneke, C., Geron, C., Goldstein, A., Graus, M., Karl, T., Kaser, L., Misztal, P., and Bin, Y.: Airborne measurements of isoprene and monoterpene emissions from southeastern US forests, *Science of the Total Environment*, 595, 149–158, <https://doi.org/10.1016/j.scitotenv.2017.03.262>, 2017.

555 Yuan, B., Kaser, L., Karl, T., Graus, M., Peischl, J., Campos, T. L., Shertz, S., Apel, E. C., Hornbrook, R. S., Hills, A., Gilman, J. B., Lerner, B. M., Warneke, C., Flocke, F. M., Ryerson, T. B., Guenther, A. B., and de Gouw, J. A.: Airborne flux measurements of methane and volatile organic compounds over the Haynesville and Marcellus shale gas production regions, *Journal of Geophysical Research: Atmospheres*, 120, 6271–6289, <https://doi.org/https://doi.org/10.1002/2015JD023242>, 2015.

Zhu, Q., Place, B., Pfannerstill, E. Y., Tong, S., Zhang, H., Wang, J., Nussbaumer, C. M., Wooldridge, P., Schulze, B. C., Arata, C., et al.: Direct observations of NO_x emissions over the San Joaquin Valley using airborne flux measurements during RECAP-CA 2021 field campaign, *Atmospheric Chemistry and Physics Discussions*, pp. 1–21, <https://doi.org/10.5194/acp-2023-3>, 2023.